Age of FGK Dwarfs Observed with LAMOST and GALAH

Sun, Tiancheng; Ge, Zhishuai; Chen, Xunzhou; Bi, Shaolan; Li, Tanda; Zhang, Xianfei; Li, Yaguang; Wu, Yaqian; Bird, Sarah A.; Ferguson, J. W.; Zhou, Jianzhao; Ye, Lifei; Long, Liu; Zhang, Jinghua

DOI:
10.3847/1538-4365/ace5b0

The Astrophysical Journal Supplement Series, 268:29 (14pp), 2023 September https://doi.org/10.3847/1538-4365/ace5b0

Age of FGK Dwarfs Observed with LAMOST and GALAH: Considering the Oxygen Enhancement

Tiancheng Sun[1,2], Zhishuai Ge[3], Xunzhou Chen[4], Shaolan Bi[1,2], Tanda Li[1,2,5], Xianfei Zhang[1,2], Yaguang Li[6], Yaqian Wu[7], Sarah A. Bird[8], J. W. Ferguson[9], Jianzhao Zhou[1,2], Lifei Ye[1,2], Liu Long[1,2], and Jinghua Zhang[7]
[1] Institute for Frontiers in Astronomy and Astrophysics, Beijing Normal University, Beijing 102206, People's Republic of China; bisl@bnu.edu.cn
[2] Department of Astronomy, Beijing Normal University, Beijing 100875, Peoples Republic of China
[3] Beijing Planetarium, Beijing Academy of Science and Technology, Beijing 100044, People's Republic of China; gezhishuai@bjp.org.cn
[4] Research Center for Intelligent Computing Platforms, Zhejiang Laboratory, Hangzhou 311100, People's Republic of China; cxz@zhejianglab.com
[5] School of Physics and Astronomy, University of Birmingham, Birmingham, B15 2TT, UK
[6] Sydney Institute for Astronomy (SIfA), School of Physics, University of Sydney, NSW 2006, Australia
[7] Key Laboratory of Optical Astronomy, National Astronomical Observatories, Chinese Academy of Sciences, A20 Datun Road, Chaoyang District, Beijing 100101, Peoples Republic of China
[8] Center for Astronomy and Space Sciences, China Three Gorges University, Yichang 443002, People's Republic of China
[9] Department of Physics, Wichita State University, Wichita, KS 67260-0032, USA
Received 2022 November 28; revised 2023 July 7; accepted 2023 July 8; published 2023 September 7

Abstract

Varying oxygen abundance could impact modeling-inferred ages. This work aims to estimate the ages of dwarfs considering observed oxygen abundance. To characterize 67,503 LAMOST and 4006 GALAH FGK-type dwarf stars, we construct a grid of stellar models, which take into account oxygen abundance as an independent model input. Compared with ages determined with commonly used α-enhanced models, we find a difference of $\sim$9% on average when the observed oxygen abundance is considered. The age differences between the two types of models are correlated to [Fe/H] and [O/α], and they are relatively significant on stars with [Fe/H] $\lesssim -0.6$ dex. Generally, varying 0.2 dex in [O/α] will alter the age estimates of metal-rich ($-0.2 <$ [Fe/H] < 0.2) stars by $\sim$10% and relatively metal-poor ($-1 <$ [Fe/H] < -0.2) stars by $\sim$15%. Of the low-O stars with [Fe/H] < 0.1 dex and [O/α] ~ -0.2 dex, many have fractional age differences of $\geqslant$ 10% and even reach up to 27%. The fractional age difference of high-O stars with [O/α] $\sim$0.4 dex reaches up to -33% to -42% at [Fe/H] $\lesssim -0.6$ dex. We also analyze the chemical properties of these stars. We find a decreasing trend of [Fe/H] with ages from 7.5–9 Gyr to 5–6.5 Gyr for the stars from the LAMOST and GALAH. The [O/Fe] of these stars increases with decreasing age from 7.5–9 Gyr to 3–4 Gyr, indicating that the younger population is more O rich.

Unified Astronomy Thesaurus concepts: Stellar abundances (1577); Stellar ages (1581); Stellar kinematics (1608); Milky Way disk (1050); Fundamental parameters of stars (555)

1. Introduction

Galactic archeology uses the chemical abundances, kinematics, and derived ages of resolved stellar populations as fossils to investigate the formation and evolution history of the Milky Way (Freeman & Bland-Hawthorn 2002; Helmi 2020). However, in comparison to chemical abundance and kinematics estimation, estimating the ages of field stars is a challenging task due to the inherent uncertainties present in both observational data and the stellar models employed for dating stars (Soderblom 2010).

The chemical composition of a star is a fundamental input parameter in the construction of its theoretical model, which is critical in the determination of its age. Notably, at fixed [Fe/H], the abundance variations of individual elements exert a consequential impact on the overall metallicity Z, which subsequently determines the opacity of the stellar models. This, in turn, influences the efficiency of energy transfer and the thermal structure, thereby altering the evolution tracks on the H-R diagram and the main-sequence (MS) lifetime (e.g., VandenBerg et al. 2012; Chen et al. 2022). Consequently, in the context of stellar modeling, it is essential to consider the proper metal mixture in order to accurately characterize stars and determine their ages. The solar-scaled ([α/Fe] = 0) and α-enhanced mixtures (αEMs) have been commonly used in theoretical model grids like Y2 isochrones (Yi et al. 2001; Kim et al. 2002; Yi et al. 2003; Demarque et al. 2004), Dartmouth Stellar Evolution Database (Dotter et al. 2008), and Padova stellar models (Girardi et al. 2000; Salasnich et al. 2000; Bressan et al. 2012; Fu et al. 2018). These models treated all the α elements, which are O, Ne, Mg, Si, S, Ca, and Ti, by the same factor.

Observations from high-resolution spectroscopic data have presented very different O-enhancement values from other α elements on many stars (Bensby et al. 2005; Reddy et al. 2006; Nissen et al. 2014; Bertran de Lis et al. 2015; Amarsi et al. 2019). The observed discrepancies in the abundances of oxygen and other α elements can be attributed to the diverse origins of these elements. Specifically, O and Mg are believed to be primarily synthesized during the hydrostatic burning phase of massive stars and subsequently ejected by the core-collapse supernovae (CCSNe; e.g., Wheeler et al. 1989; Kobayashi et al. 2006, 2020). Nevertheless, some works have provided evidence that Mg might also be partially released into the interstellar medium by SNe Ia (Magrini et al. 2017; Naiman et al. 2018; Ventura et al. 2018; Franchini et al. 2021), while O appears to be solely enriched by CCSNe (Franchini et al. 2021). The other α elements, namely Si, Ca, and Ti, primarily

originate from the explosive burning of CCSNe and are partially contributed by SNe Ia (e.g., Carigi et al. 2005; Maoz et al. 2012; Kobayashi et al. 2020). For instance, 22% of Si and 39% of Ca come from SNe Ia according to the chemical evolution models in Kobayashi et al. (2020). Therefore, not all α elements vary in lockstep; the abundance of oxygen may not necessarily correlate with the abundance of other α elements.

Many works have also discussed the effects of varying individual element abundances on the stellar evolution models (Dotter et al. 2007; Pietrinferni et al. 2009; VandenBerg et al. 2012; Beom et al. 2016). Theoretical models showed that the oxygen abundance influences the stellar evolution differently from the other α elements (Vandenberg 1992; VandenBerg et al. 2012). Furthermore, Ge et al. (2016) proposed the CO-extreme models, which treat oxygen abundance differently from the other α elements and add carbon abundance in the stellar evolution models. The models have been employed to determine the ages of thousands of metal-poor halo stars, disk stars, and MS turn-off stars (Ge et al. 2016; Chen et al. 2020, 2022). These results showed that increasing oxygen abundance leads to smaller age determination for the stars with [Fe/H] < -0.2. For the stars with [Fe/H] < -0.2 and [O/α] > 0.2 dex, the age difference would be about 1 Gyr. Due to the limited sample sizes of previous studies (Ge et al. 2016, with 70 stars, and Chen et al. 2020, with 148 stars) or the restricted range of [Fe/H] values ([Fe/H] $\gtrsim -0.1$ dex; Chen et al. 2022), there is a pressing need for a large and self-consistent sample to conduct a quantitative analysis regarding the impact of O enhancement on age determination.

Recently, millions of stars' individual element abundances have been measured by spectroscopic surveys like LAMOST (Large Sky Area Multi-Object Fiber Spectroscopic Telescope; Deng et al. 2012; Zhao et al. 2012; Liu et al. 2014; Luo et al. 2015), APOGEE (Majewski et al. 2017), and GALAH (Galactic Archaeology with HERMES; De Silva et al. 2015; Buder et al. 2021). These large sky surveys provide an excellent opportunity to study the effects of oxygen abundance variations on age determinations across a wide range of stellar parameters. To investigate the systematic effects of O enhancement on age determination, we study the dwarf stars with available oxygen abundance measurements from LAMOST and GALAH. This paper is organized as follows: Section 2 mentions the data selection; Section 3 describes computations of stellar model grids; Section 4.1 demonstrates age differences between the O-enhanced models and α-enhanced models; the resulting age–abundance trends are presented in Section 4.2; and the conclusions of this work are drawn in Section 5.

2. Target Selection

In this work, we make use of spectroscopic data from LAMOST Data Release 5 (DR5) value-added catalog (VAC; Xiang et al. 2019) and third data release (DR3) of GALAH (Buder et al. 2021), together with astrometric data from Gaia Data Release 3 (Gaia Collaboration et al. 2023).

2.1. Spectroscopic Data

The LAMOST DR5 VAC (Xiang et al. 2019) contains more than 6 million stars with atmosphere parameters ($T_{\rm eff}$, $\log g$, $V_{\rm mic}$) and chemical abundances of 16 elements (C, N, O, Na, Mg, Al, Si, Ca, Ti, Cr, Mn, Fe, Co, Ni, Cu, and Ba). Measurements of element abundances are based on the DDPayne tool (Ting et al. 2017; Xiang et al. 2019), which is a data-driven method that incorporates constraints from theoretical spectral models. It is noteworthy that, as discussed by Ting et al. (2018), the direct derivation of oxygen abundances from atomic oxygen lines or oxygen-bearing molecular lines in low-resolution ($R \sim$1800) LAMOST spectra is unfeasible. Alternatively, CH and CN molecular lines can be utilized for indirect estimation of oxygen abundances as their strengths are sensitive to the amount of carbon locked up in CO molecules. As a result, the LAMOST oxygen abundances are only available in the cooler stars ($T_{\rm eff} \lesssim$5700 K), where the CH and CN lines have sufficient strength to allow a reasonably precise ($\pm$0.10 dex) estimate of [O/Fe] (Xiang et al. 2019). Due to the wide age range and the preservation of initial chemical abundances, the MS star could be a good tracer of stellar populations. Therefore, we select the MS stars with available measurements for [Fe/H], [α/Fe], and [O/Fe] from the catalog. First, we use some recommended labels ($T_{\rm eff}$_ flag $= 1$, $\log g$_ flag $= 1$, [Fe/H]_ flag $= 1$, [X/Fe]_ flag[10] $= 1$, qflag _ chi2 $=$ good) to select stars with reliable measurements. Afterward, we remove stars with $T_{\rm eff}$ smaller than 5000 K or signal-to-noise ratio (S/N) less than 50 because their [O/Fe] determinations are not robust. Xiang et al. (2019) also provided a tag named qflag _ singlestar to infer whether a star is single or belongs to a binary system. The tag is determined by the deviation significance of the spectroscopic parallax from the Gaia astrometric parallax. When the deviation is less than 3σ, it suggests an object is a single star. We use this tag to remove all candidate binaries from our sample. Finally, we choose stars with $\log g > 4.1$. We lastly select a total of 187,455 unique stars.

GALAH DR3 (Buder et al. 2021) presents stellar parameters ($T_{\rm eff}$, $\log g$, [Fe/H], $V_{\rm mic}$, $V_{\rm broad}$, and $V_{\rm rad}$) and up to 30 elemental abundances for 588,571 stars, derived from optical spectra at a typical resolution of $R \sim$28,000. The oxygen abundance from GALAH DR3 was calculated using the O_I 777 nm triplet (Amarsi et al. 2018), based on a non–local thermodynamic equilibrium (NLTE) method (Amarsi et al. 2020). This NLTE method has also been employed for the measurement of [Fe/H] in GALAH. Following the recommendations in GALAH DR3, we require an S/N > 30 and a quality flag $= 0$ for reliable stellar parameter determination including iron, α elements, and oxygen abundances (flag _ sp $= 0$, flag _ fe_h$= 0$, flag _ alpha _ fe $= 0$, and flag _ o _ fe $= 0$). Additionally, the sample is limited to the stars with e_ alpha _ fe < 0.1 and e_ o _ fe < 0.1. We exclude the binary systems identified by Traven et al. (2020; which is a catalog of FGK binary stars in GALAH). These cuts give us a sample of 19,512 dwarf stars ($\log g > 4.1$).

2.2. Astrometric Data

We crossmatch our selected LAMOST and GALAH samples with the Gaia DR3 (Gaia Collaboration et al. 2023) catalog to obtain the luminosity for each star. Given that luminosity is utilized as a key observational constraint for estimating stellar age, we select stars with luminosity uncertainty less than 10%. Additionally, we select single stars by making a cut based on the Gaia renormalized unit weight error (RUWE) being less

[10] [X/Fe]_ flag $= 1$ for 14 elements (C, N, O, Na, Mg, Al, Si, Ca, Ti, Cr, Mn, Fe, Co, and Ni).

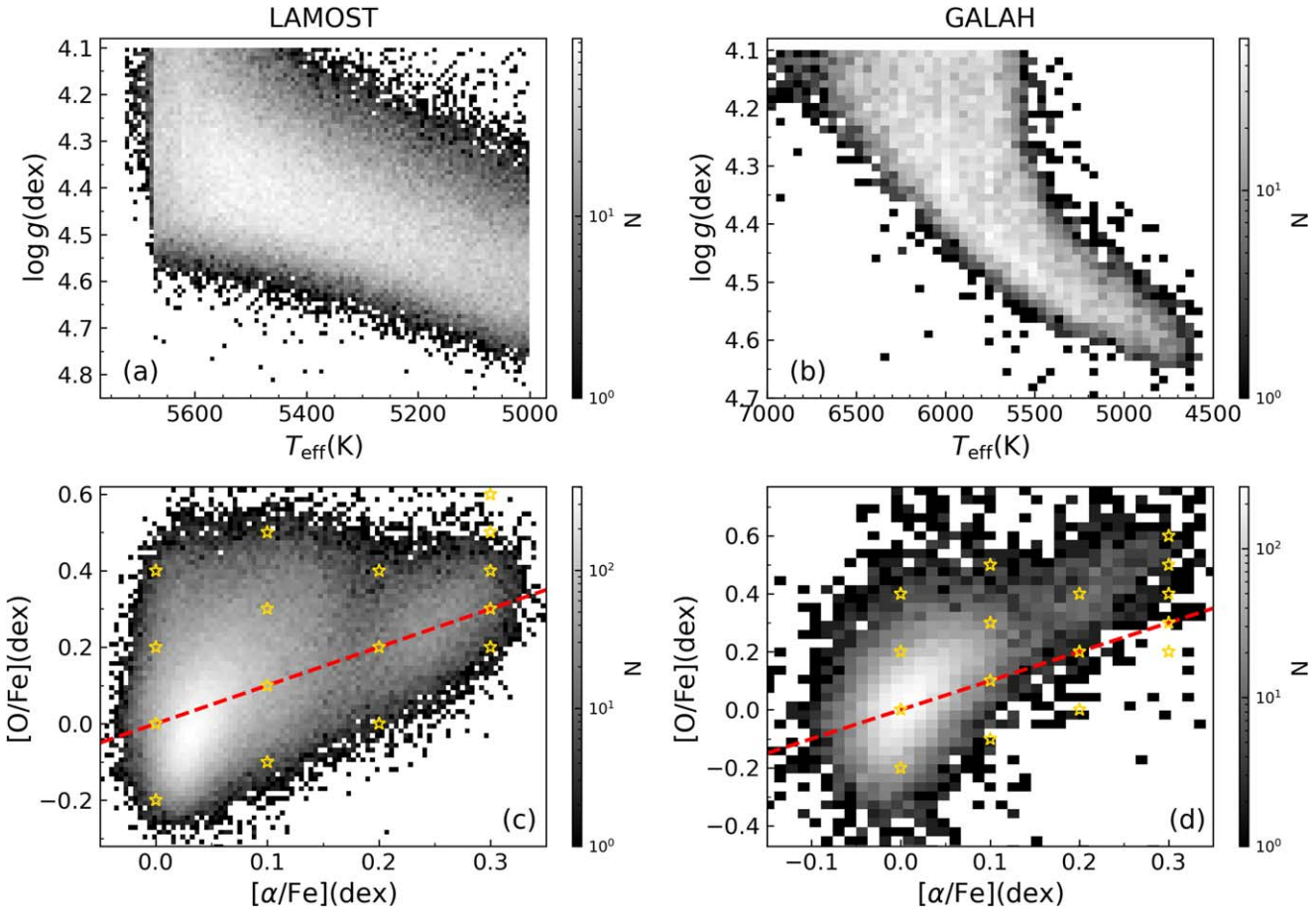

Figure 1. Color-coded stellar number density distributions of the targets from LAMOST (left column) and GALAH (right column) in the Kiel diagram ((a)–(b)) and the [α/Fe]–[O/Fe] space ((c)–(d)). The red dashed lines in panels (c)–(d) indicate the 1:1 relation. The gold pentagrams represent the input metal mixtures (shown in Table 2) of the stellar model grid.

than 1.2 (RUWE values are from the Gaia DR3). Our final sample consists of 149,906 stars from LAMOST (5000 K $<$ $T_{\rm eff}$ $<$ 5725 K, -1 $<$ [Fe/H] $<$ 0.5, $\log g >$ 4.1) and 15,591 stars from GALAH (4500 K $<$ $T_{\rm eff}$ $<$ 7000 K, -1 $<$ [Fe/H] $<$ 0.5, $\log g >$ 4.1).

We calculate the Galactic Cartesian coordinates (X, Y, Z) and velocities (U, V, W) for the LAMOST sample using the Python package Galpy (Bovy 2015). The distances are estimated by Bailer-Jones et al. (2021). The Sun is located at (X, Y, Z)= (-8.3, 0, 0) kpc, and the solar motion with respect to the local standard of rest is ($U_\odot$, $V_\odot$, $W_\odot$) = (11.1, 12.24, 7.25) km s^{-1} (Schönrich et al. 2010). We use the Galactic Cartesian coordinates and velocities from the GALAH DR3 VAC, which is based on astrometry from Gaia EDR3 and radial velocities determined from the GALAH spectra (Zwitter et al. 2021).

In Figure 1, we demonstrate dwarfs from LAMOST and GALAH in the Kiel diagram and the [α/Fe][11]-[O/Fe] space to inspect their general distributions. The Kiel diagram in Figure 1(a) shows that most of the LAMOST dwarfs are cooler than 5700 K, while the GALAH dwarfs in Figure 1(b) covers a wider range of $T_{\rm eff}$ (4500–7000 K). It should be noted that we do not apply any cutoff value at the high-temperature side for the LAMOST sample. This upper limit is where reliable oxygen abundance can be measured by Xiang et al. (2019). The [α/Fe]-[O/Fe] diagrams in Figure 1(c), (d) show that the [O/Fe] generally increases with increasing [α/Fe]; however, [O/Fe] widely spreads at given α-enhanced values. The spreading is relatively large for low-α stars (especially for the GALAH sample), ranging from -0.4 to $+0.6$.

[11] The [α/Fe] from both the LAMOST and GALAH catalog are defined as an error-weighted mean of [Mg/Fe], [Si/Fe], [Ca/Fe], and [Ti/Fe].

3. Stellar Models

3.1. Input Physics

We construct a stellar model grid using the Modules for Experiments in Stellar Astrophysics (MESA) code (Paxton et al. 2011, 2013, 2015, 2018, 2019). The versions of MESA and MESA SDK we used are Revision 12115 and Version 20.3.1, respectively.

The equation-of-state (EOS) tables in MESA are a blend of OPAL (Rogers & Nayfonov 2002), SCVH (Saumon et al. 1995), PTEH (Pols et al. 1995), HELM (Timmes & Swesty 2000), and Potekhin–Chabrier (PC; Potekhin & Chabrier 2010) EOS tables. Nuclear reaction rates are a combination of rates from NACRE (Angulo et al. 1999) and JINA REACLIB (Cyburt et al. 2010), plus additional tabulated weak-reaction rates (Fuller et al. 1985; Oda et al. 1994; Langanke & Martínez-Pinedo 2000). Screening is included via the prescription of Chugunov et al. (2007). Thermal neutrino loss rates are from Itoh et al. (1996). The helium-enrichment law is calibrated with initial abundances of helium and heavy elements of the solar model given by Paxton et al. (2011), and

Table 1
Metal Mixtures for the GS98 Solar Mixture, the α-enhanced Mixture, and the O-enhanced Mixture

Element	$\log N_{\odot}$	$\log N_{\alpha EM}$	$\log N_{OEM}$
C	8.52	8.52	8.52
N	7.92	7.92	7.92
O	8.83	8.83+[α/Fe]	8.83+[O/Fe]
F	4.56	4.56	4.56
Ne	8.08	8.08+[α/Fe]	8.08+[α/Fe]
Na	6.33	6.33	6.33
Mg	7.58	7.58+[α/Fe]	7.58+[α/Fe]
Al	6.47	6.47	6.47
Si	7.55	7.55+[α/Fe]	7.55+[α/Fe]
P	5.45	5.45	5.45
S	7.33	7.33+[α/Fe]	7.33+[α/Fe]
Cl	5.50	5.50	5.50
Ar	6.40	6.40	6.40
K	5.12	5.12	5.12
Ca	6.36	6.36+[α/Fe]	6.36+[α/Fe]
Sc	3.17	3.17	3.17
Ti	5.02	5.02+[α/Fe]	5.02+[α/Fe]
V	4.00	4.00	4.00
Cr	5.67	5.67	5.67
Mn	5.39	5.39	5.39
Fe	7.50	7.50	7.50
Co	4.92	4.92	4.92
Ni	6.25	6.25	6.25

it results in $Y = 0.248 + 1.3324\ Z$. The mixing-length parameter α_{MLT} is fixed to 1.82. Microscopic diffusion and gravitational settling of elements are necessary for stellar models of low-mass stars, which will lead to a modification to the surface abundances and MS lifetimes (e.g., Chaboyer et al. 2001; Bressan et al. 2012). Therefore, we include diffusion and gravitational settling using the formulation of Thoul et al. (1994). We use the solar mixture GS98 from Grevesse & Sauval (1998). The opacity tables are OPAL high-temperature opacities[12] supplemented by the low-temperature opacities (Ferguson et al. 2005).

We customize metal mixtures by introducing two enhancement factors: one for oxygen and one for all other α elements (i.e., Ne, Mg, Si, S, Ca, and Ti). The two factors are applied in the same way as Ge et al. (2015) to vary the volume density of element ($\log N$) based on the GS98 solar mixture as presented in Table 1. We make a number of opacity tables by varying two enhancement factors according to the ranges of [α/Fe] and [O/Fe] values of the star sample. The enhancement values are shown in Table 2. For the mixtures with the same oxygen and α-elements enhancement factors, we refer to them as αEM; otherwise, we refer to them as O-enhanced mixture (OEM).

3.2. Grid Computations

We establish stellar model grids that include various metal-mixture patterns as indicated in Table 2. The mass range is from 0.6 to 1.2 $M_{\odot}$ with a grid step of 0.02 $M_{\odot}$. Input [Fe/H] values range from -1.20 to $+0.46$ dex with a grid step of 0.02 dex. The computation starts at the Hayashi line and terminates at the end of MS when core hydrogen exhausts (mass fraction of center hydrogen goes below 10^{-12}). The inlist file (for MESA) utilized in the computation of our stellar models is available on Zenodo at doi:10.5281/zenodo.7866625.

[12] http://opalopacity.llnl.gov/new.html

Table 2
Grid of Evolutionary Models with Two Metal-mixture Patterns

Metal Mixture	(O/Fe) (dex)	(α/Fe) (dex)
O-enhanced mixture	−0.2	0
	0.2	0
	0.4	0
	−0.1	0.1
	0.3	0.1
	0.5	0.1
	0	0.2
	0.4	0.2
	0.2	0.3
	0.4	0.3
	0.5	0.3
	0.6	0.3
α-enhanced mixture	0	0
	0.1	0.1
	0.2	0.2
	0.3	0.3

Table 3
Z Values of Fixed [Fe/H] with Two Metal-mixture Patterns

(Fe/H) (dex)	(α/Fe) (dex)	(O/Fe) (dex)	Z (dex)
−1.0	0.1	0.1	0.0020
−1.0	0.1	0.5	0.0036
−0.8	0.1	0.1	0.0032
−0.8	0.1	0.5	0.0056
−0.6	0.1	0.1	0.0051
−0.6	0.1	0.5	0.0089
−0.4	0.1	0.1	0.0080
−0.4	0.1	0.5	0.0139
−0.2	0.1	0.1	0.0126
−0.2	0.1	0.5	0.0217
0	0.1	0.1	0.0197
0	0.1	0.5	0.0337

To explicate the effect of oxygen enhancement on the evolutionary tracks, we provide an exposition of representative evolutionary tracks in Figure 2. The corresponding values of Z are listed in Table 3. At fixed [Fe/H], the variation of [O/Fe] would influence opacity, which could influence the energy transfer efficiency and the thermal structure. We find that the larger [O/Fe] leads to higher opacity at input [Fe/H] $\leqslant -0.2$ and shifts the evolutionary tracks to lower $T_{\rm eff}$. As seen in Figure 2, at [Fe/H] $\leqslant -0.2$, O-rich models are generally cooler than the α-enhanced models at given input [Fe/H], leading to higher modeling-determined masses (smaller ages) for a given position on the H-R diagram (left panel of Figure 3). However, at input [Fe/H] $= 0$, larger [O/Fe] leads to lower opacity, and shifts the evolutionary tracks to higher $T_{\rm eff}$. The O-rich models are slightly hotter than the α-enhanced models. Overall, at fixed mass, the $T_{\rm eff}$ difference between the two models becomes significant with smaller [Fe/H]. In addition, we note that the 1.1 $M_{\odot}$ and 1.2 $M_{\odot}$ tracks of O-rich models show different behavior compared with the tracks of 0.7–1.0 $M_{\odot}$. The O-rich models with 1.1 $M_{\odot}$ show a blue hook morphology at

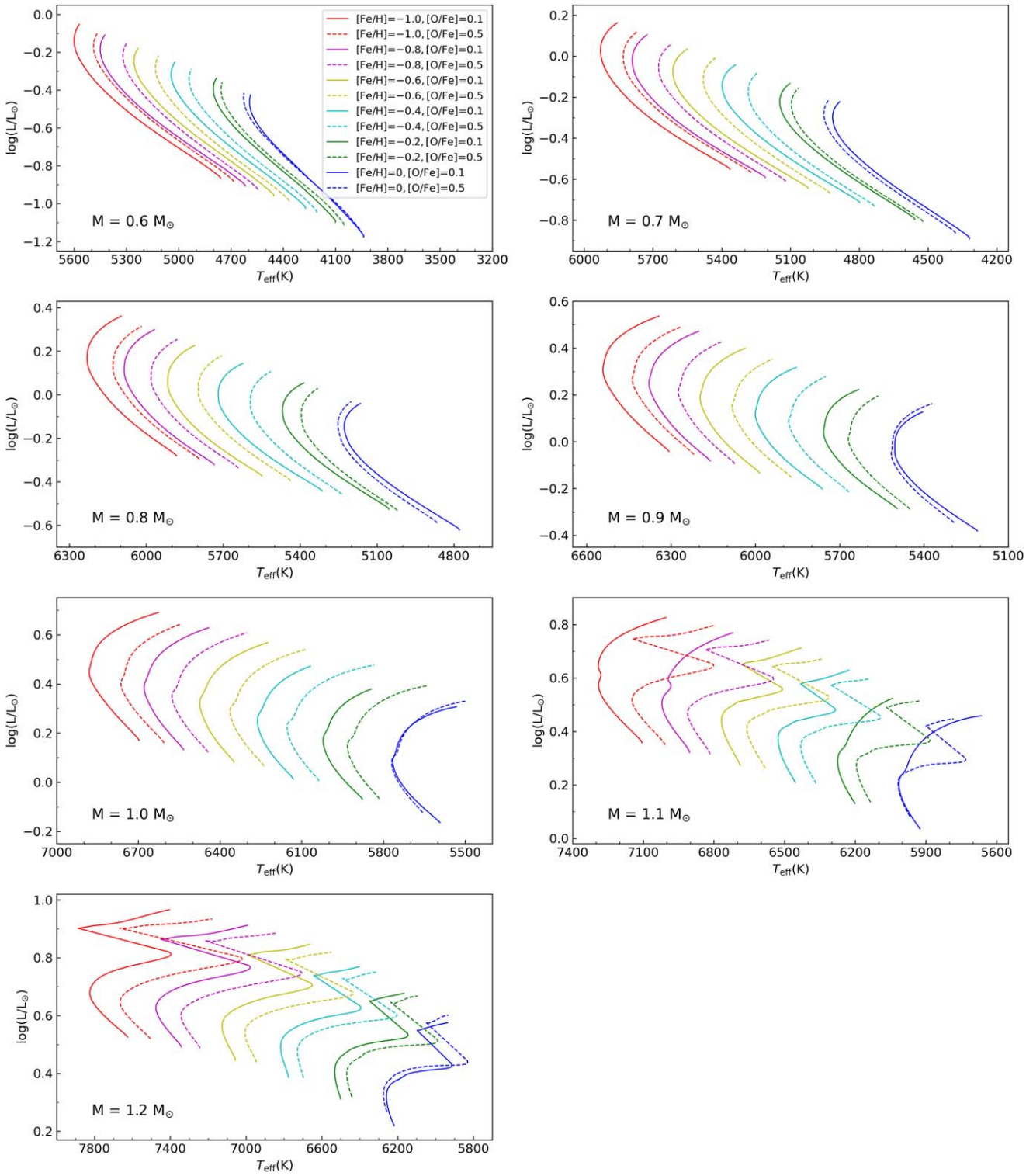

Figure 2. Stellar evolution tracks of fixed mass ($M = 0.6$, 0.7, 0.8, 0.9, 1.0, 1.1, 1.2 $M_{\odot}$) computed with αEM and OEM models. In each panel, the [Fe/H] range is 0, −0.2, −0.4, −0.6, −0.8, and −1.0 (from right to left). The solid lines and dashed lines represent the tracks with input [O/Fe] = 0.1 and 0.5, respectively. All tracks have the same input [α/Fe] (0.1 dex) values. The Z values of each track are presented in Table 3.

[Fe/H] $\leqslant -0.8$, which enlarges the $T_{\rm eff}$ difference between two models at this evolutionary phase. At 1.2 $M_{\odot}$, both models show a blue hook morphology at the end of MS, and the $T_{\rm eff}$ difference keeps approximately constant at [Fe/H] $\leqslant -0.6$.

Figure 3 presents the stellar evolution tracks of two example stars calculated with αEM and OEM models. Figure 3(a) presents the tracks of a star with observed [α/Fe] $\sim$0.1, [O/Fe] $\sim$0.5. Based on the αEM models (input [α/Fe] = 0.1, [O/Fe] = 0.1), we obtain the best-fit values of fundamental parameters for this star: mass = 0.87 ± 0.02 $M_{\odot}$, age = 8.69 ± 1.49 Gyr (the fitting method is described in detail in Section 3.3). Using the OEM models (input [α/Fe] = 0.1, [O/Fe] = 0.5), we estimate it to be a young star with mass = 0.90 ± 0.02 $M_{\odot}$, age = 5.68 ± 1.44 Gyr. The mean

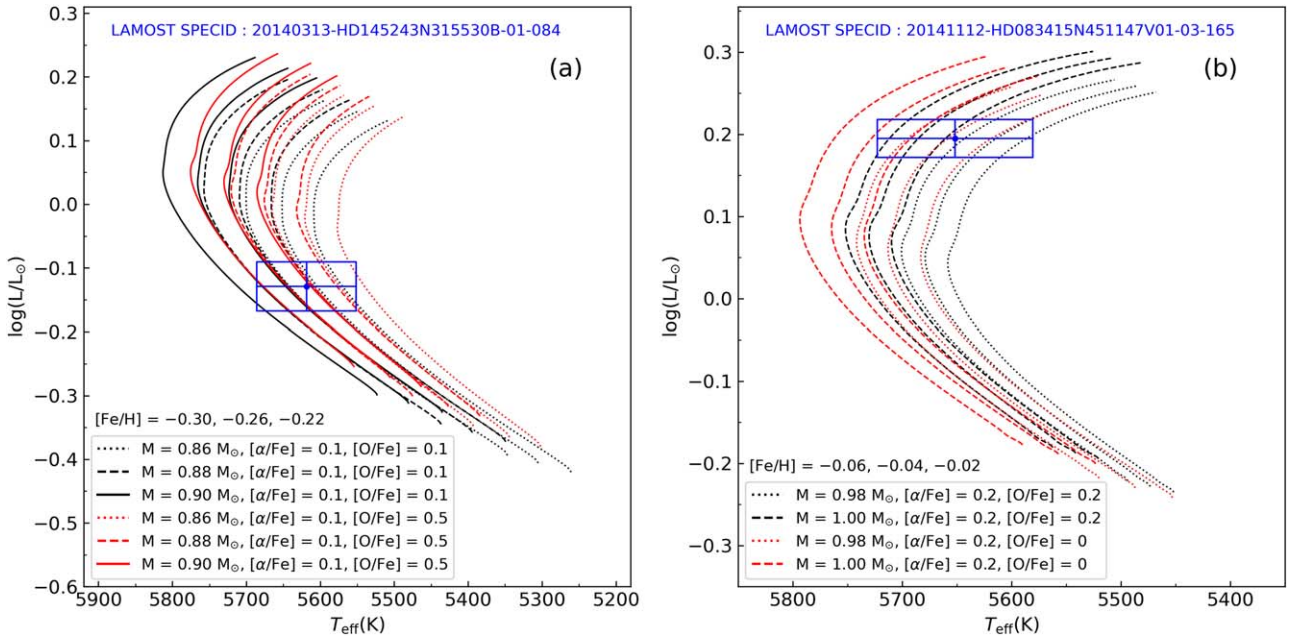

Figure 3. Stellar evolution tracks of two example stars calculated with αEM (black) and OEM (red) models. Panel (a) shows the tracks of a star with [α/Fe] $\sim$0.1 and [O/Fe] $\sim$0.5 (LAMOST SPECID: 20140313-HD145243N315530B-01-084); panel (b) shows the tracks of a star with [α/Fe] $\sim$0.2 and [O/Fe] $\sim$0 (LAMOST SPECID: 20141112-HD083415N451147V01-03-165). At fixed mass and metal mixture (fixed color and line type), the input [Fe/H] values of tracks (from left to right) are shown. The blue dots and error bars are the observed values and uncertainties of example stars, while the blue squares represent the observational error box. The atmosphere parameters and chemical abundance for these stars are shown in Table 4.

Table 4
Atmosphere Parameters and Chemical Abundance for the Example Stars from LAMOST

Star sobject _ id	$T_{\rm eff}$ (K)	(Fe/H) (dex)	Luminosity ($L_\odot$)	(α/Fe) (dex)	(O/Fe) (dex)
20140313-HD145243N315530B-01-084	5619 ± 22	-0.30 ± 0.04	0.74 ± 0.02	0.06 ± 0.02	0.46 ± 0.09
20141112-HD083415N451147V01-03-165	5652 ± 24	-0.15 ± 0.04	1.57 ± 0.03	0.15 ± 0.02	-0.02 ± 0.08

Table 5
Fundamental Parameters and Chemical Abundance for the Example Stars from GALAH

Star sobject _ id	$T_{\rm eff}$ (K)	(Fe/H) (dex)	Luminosity ($L_\odot$)	(α/Fe) (dex)	(O/Fe) (dex)	$\rm Mass_{\alpha EM}$ ($M_\odot$)	$\rm Mass_{Buder2021}$ ($M_\odot$)	$\rm Age_{\alpha EM}$ (Gyr)	$\rm Age_{Buder2021}$ (Gyr)
171230005802396	6096 ± 76	-0.23 ± 0.06	2.26 ± 0.07	0 ± 0.02	0.02 ± 0.08	1.06 ± 0.03	1.03 ± 0.04	6.08 ± 1.01	6.46 ± 1.17
160529003401378	5846 ± 76	-0.42 ± 0.06	1.67 ± 0.03	0.31 ± 0.03	0.34 ± 0.09	0.97 ± 0.03	0.96 ± 0.03	9.53 ± 1.26	10.04 ± 1.39

Note. The masses ($\rm Mass_{Buder2021}$) and ages ($\rm Age_{Buder2021}$) of the two example stars from the GALAH VAC (Buder et al. 2021) are calculated based on the PAdova and TRieste Stellar Evolution Code (PARSEC; Marigo et al. 2017) stellar isochrones.

value of masses of OEM models ([O/Fe] = 0.5) inside the observational error box is larger than that of αEM models ([O/Fe] = 0.1), leading to smaller modeling-determined age for this star. Figure 3(b) shows the tracks of a star with observed [α/Fe] $\sim$0.2, [O/Fe] $\sim$0. We obtain a mass of $0.99 \pm 0.01\ M_\odot$ and an age of 10.51 ± 0.60 Gyr for this star with αEM models (input [α/Fe] = 0.2, [O/Fe] = 0.2) and a mass of $0.98 \pm 0.02\ M_\odot$ and an age of 11.34 ± 0.51 Gyr with OEM models (input [α/Fe] = 0.2, [O/Fe] = 0). As seen, the OEM models with input [O/Fe] = 0 are generally hotter than the αEM models ([O/Fe] = 0.2) at fixed mass and [Fe/H], leading to smaller modeling-determined mass and larger age for this star.

3.3. Fitting Method

We constrain stellar masses and ages using five observed quantities, i.e., $T_{\rm eff}$, luminosity, [Fe/H], [α/Fe], and [O/Fe]. Note that [O/Fe] is not used when estimating parameters with αEM models.

We follow the fitting method raised by Basu et al. (2010). According to the Bayes theorem, we compare model predictions with their corresponding observational properties D to calculate the overall probability of the model M_i with posterior probability I,

$$p(M_i|D, I) = \frac{p(M_i|I)p(D|M_i, I)}{p(D|I)}, \quad (1)$$

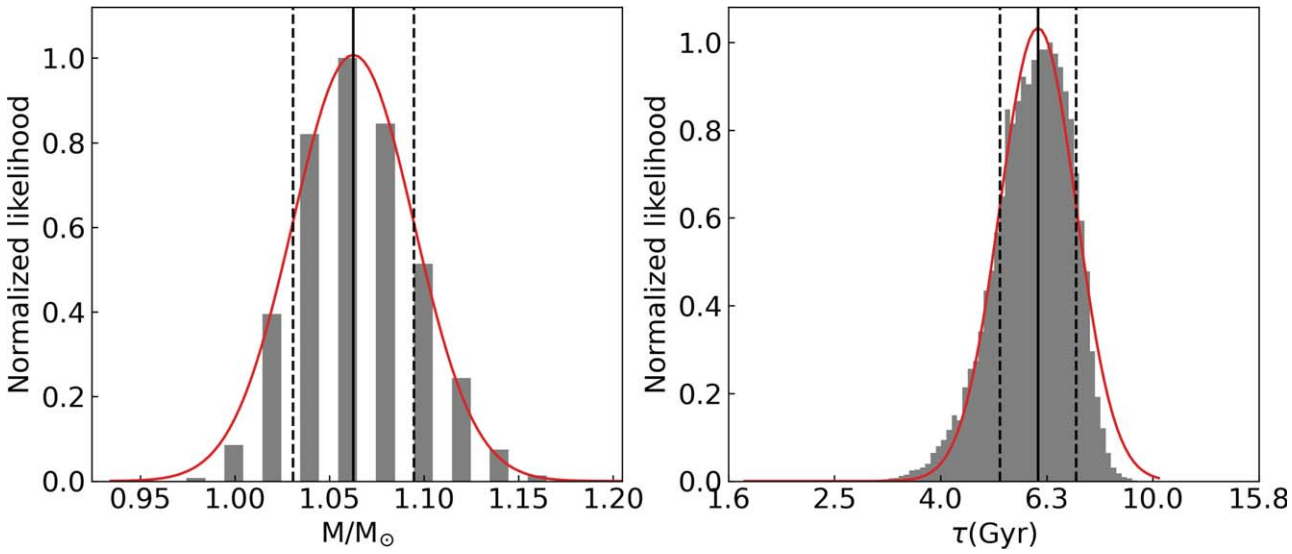

(a) GALAH sobject_id: 171230005802396

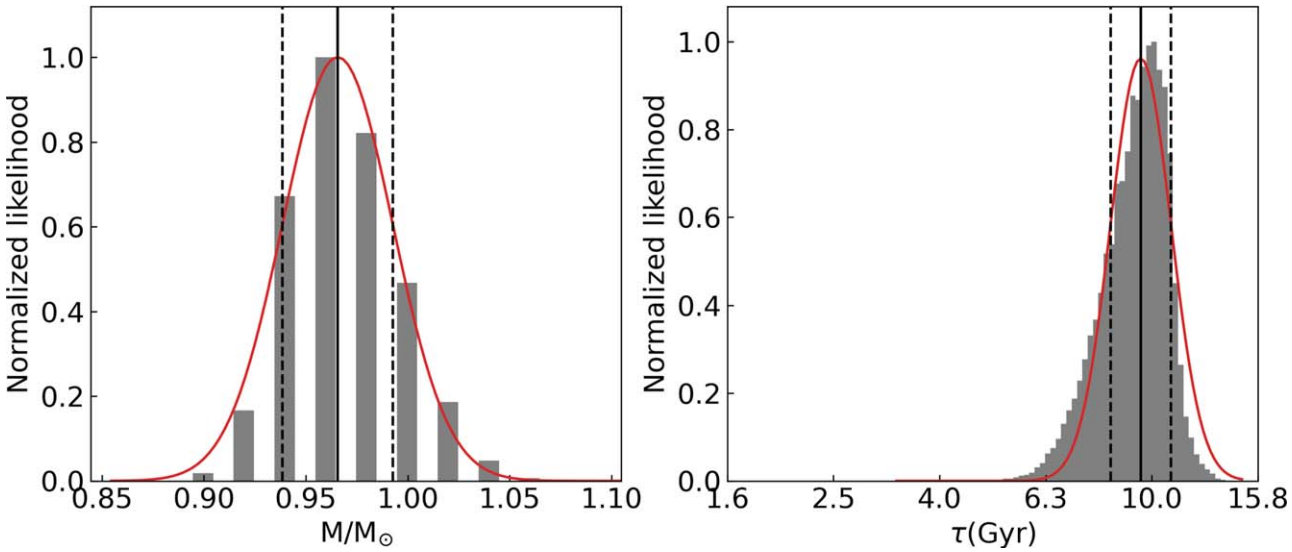

(b) GALAH sobject_id: 160529003401378

Figure 4. Likelihood distributions of mass and age for two example stars from GALAH. The red solid line represents the Gaussian function that fits to the likelihood distribution. Solid and dashed vertical lines indicate the mean and standard deviation of the Gaussian profile. The fundamental parameters and chemical abundance for these stars are shown in Table 5.

where $p(M_i\ |I)$ represents the uniform prior probability for a specific model, and $p(\mathrm{D}\ |M_i, I)$ is the likelihood function:

$$p(D|M_i, I) = L(T_{\mathrm{eff,[Fe/H],lum}}) = L_{T_{\mathrm{eff}}} L_{[Fe/H]} L_{\mathrm{lum}}. \quad (2)$$

The $p(D|I)$ in Equation (1) is a normalization factor for the specific model probability:

$$p(D|I) = \sum_{j=1}^{N_m} p(M_j|I)p(D|M_j, I), \quad (3)$$

where N_m is the total number of selected models. The uniform priors $p(M_i\ |I)$ can be canceled, giving the simplified Equation (1) as

$$p(M_i|D, I) = \frac{p(D|M_i, I)}{\sum_{j=1}^{N_m} p(D|M_j, I)}. \quad (4)$$

Then Equation (4) is the probability distribution for the selected models with the most probable fundamental parameters. As demonstrated in Figure 4, we fit a Gaussian function to the likelihood distribution of mass and age for each star. The mean and standard deviation of the resulting Gaussian profile are then utilized as the median value and uncertainty of fundamental parameter (mass and age) for each star. To find the stars that locate near the edge of the model grid, we consider a 3σ error

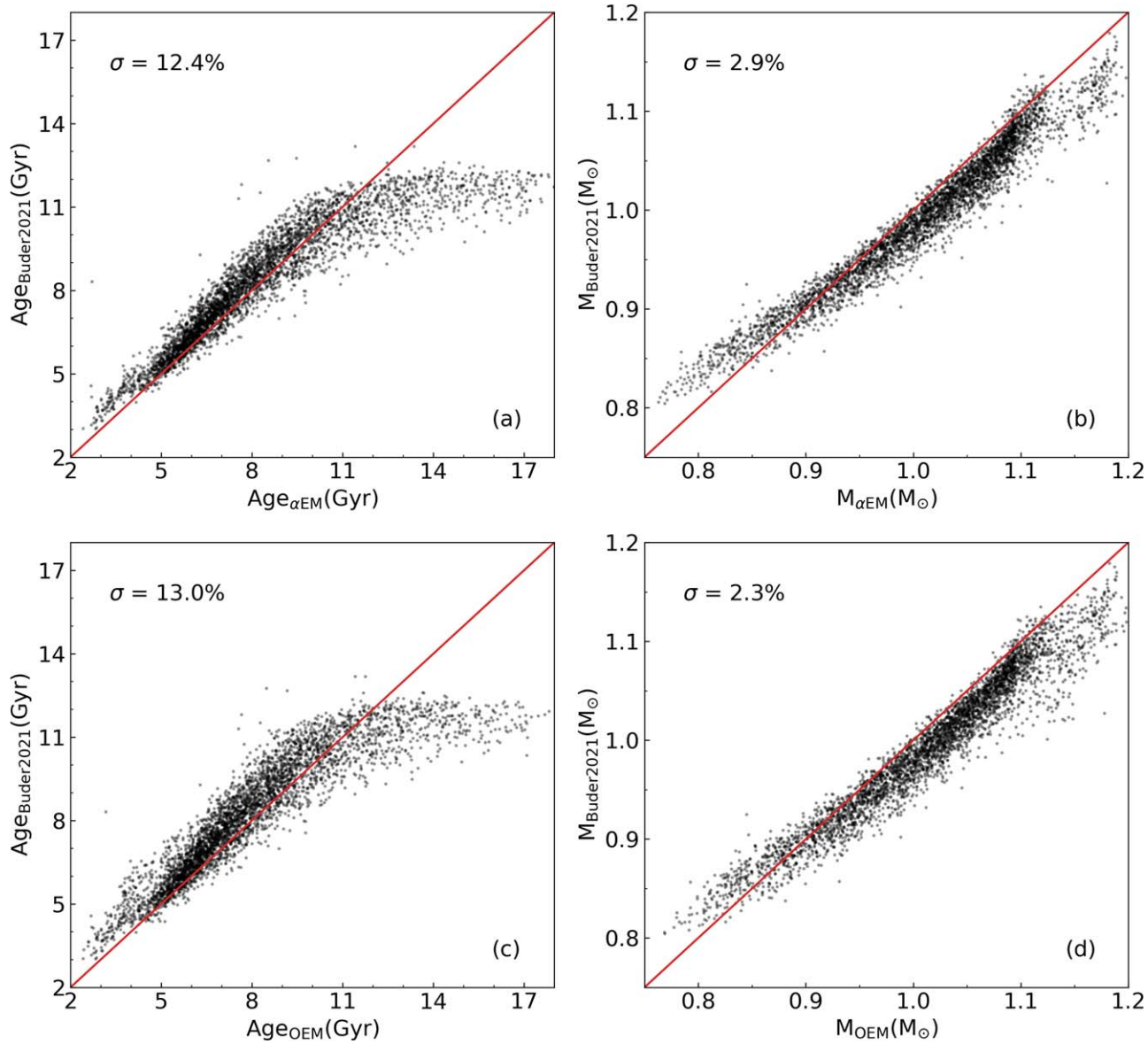

Figure 5. Comparison of masses and ages of ∼4000 GALAH sample stars from our α EM models, OEM models, and the GALAH DR3 VAC (Buder et al. 2021). The red line represents the 1:1 line. Dispersion of the relative age and mass difference is marked in the figure.

box (i.e., 3 times the observational error, depicted as a blue square in Figure 3) on the H-R diagram and divide the error box into 100 bins. For a certain star, when there are more than five bins that do not contain any theoretical model (sampling rate $< 95\%$), we flag the star with "edge effect."

To assess the accuracy of our models and investigate potential model dependency in age and mass determination, we present a comparison of results obtained from our αEM models, OEM models, and the GALAH DR3 VAC (Buder et al. 2021). Figure 5 shows the comparison of age and mass estimations for ∼4000 GALAH stars, with age uncertainty of less than 30%, based on αEM models, OEM models, and GALAH DR3 VAC (Buder et al. 2021). The ages and masses of stars from GALAH DR3 VAC are calculated using the PARSEC release v1.2S + COLIBRI stellar isochrones (Marigo et al. 2017), which adopt a solar-scaled metal mixture, i.e., input $[\alpha/\mathrm{Fe}] = 0$. Figure 5 illustrates that the one-to-one relation of the results is quite good for most stars. It is noteworthy that the adopted approach encompasses a flat prior on age with an age cap of 13.2 Gyr (Sharma et al. 2018). Consequently, the ages of the majority of stars from GALAH DR3 VAC are found to be younger than 12 Gyr (with masses larger than 0.8 $M_{\odot}$), which results in a relatively large dispersion of age differences, amounting to 12.4% for αEM models and 13.0% for OEM models. Significant systematic differences are apparent between the PARSEC and the αEM models in Figures 5(a)–(b), with the former indicating 2.3% older age and 1.5% smaller mass than the latter. These discrepancies could be attributed to differences in the input physics employed by the two models, such as the input $[\alpha/\mathrm{Fe}]$ value, helium abundance, and mixing-length parameter. In Figures 5(c)–(d), the PARSEC yields 5.5% older age and 1.9% smaller mass than the OEM models. Compared with the αEM models, the OEM models demonstrate more pronounced systemic differences from PARSEC. These distinctions primarily arise from the consideration of O enhancement in OEM models, leading to younger ages and higher masses. In addition, a comparison of results obtained from our α EM

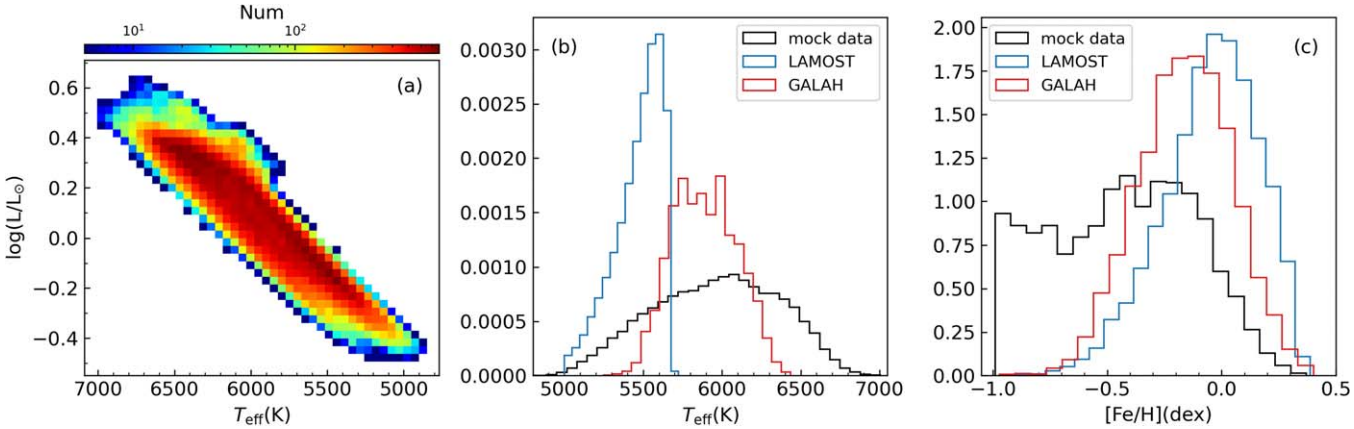

Figure 6. Panel (a) shows the color-coded stellar number density distributions of mock stars on the H-R diagram. Panels (b)–(c) show the comparison of $T_{\rm eff}$ and [Fe/H] distributions between mock data and observational data.

models and the YonsiYale (YY; Yi et al. 2008) stellar isochrones have been shown in Figure 11 in the Appendix.

4. Results

This work aims to determine the ages of dwarfs considering oxygen abundance and study the chemical and kinematic properties of high-α and low-α populations in the Galactic disk. We give the masses and ages of 149,906 LAMOST dwarfs and 15,591 GALAH dwarfs with α EM models and OEM models. We remove $\sim$30% stars with sampling rate $<$ 95%, located near the edge of the model grid. In addition, we remove $\sim$3% stars whose inferred ages are 2σ larger[13] than the Universe age (13.8 Gyr; Planck Collaboration et al. 2016) due to their significant model systematic bias. Finally, we remove $\sim$35% stars that have relative age uncertainty larger than 30%. After these cuts, we obtain the ages of 67,503 dwarfs from LAMOST with a median age uncertainty of $\sim$16% and 4006 dwarfs from GALAH with a median age uncertainty of $\sim$18%. The age estimation of dwarf stars is inherently accompanied by considerable uncertainty, which can reach up to 30% within our sample. Furthermore, uncertainties (especially the systematic error) in atmosphere parameters can introduce biases in the age estimation. Consequently, a minority of stars in our sample exhibits ages that exceed the age of the Universe. This occurrence is not uncommon as even samples of subgiants with more precise age determinations have encountered analogous occurrences (Xiang & Rix 2022).

4.1. Oxygen Effect on Age Determinations

4.1.1. Mock Data Test

Most of the stars in both the LAMOST and GALAH samples are distributed in a relatively narrow range of [Fe/H] (-0.5 to $+0.5$ dex). To systematically investigate the effect of O enhancement on age determinations in a wide range of $T_{\rm eff}$ and [Fe/H], we apply a mock data test based on our grid of stellar models. For each set of stellar mode grids with fixed [Fe/H], [α/Fe], and [O/Fe] values, we draw random samples from the distributions of stellar evolution tracks in the H-R diagram. We adopt 0.05, 30 K as the observational errors for [Fe/H] and $T_{\rm eff}$ and fractional error of 2% for luminosity. Finally, we generate mock data of 0.15 million stars with age uncertainty of less than 30%.

Figure 6(a) shows the distribution of mock stars on the H-R diagram. Figures 6(b)–(c) present a comparison between mock data and observational data for $T_{\rm eff}$ and [Fe/H] distributions. Comparing mock data with LAMOST or GALAH dwarfs, mock stars cover wider ranges of $T_{\rm eff}$ (5000–7000 K) and [Fe/H] (-1.0 to $+0.4$ dex). Therefore, the mock data are useful for statistical studies of oxygen effect on age determinations.

Figure 7 shows a comparison between ages determined with α EM models ($\tau_{\alpha\rm EM}$) and OEM models ($\tau_{\rm OEM}$). The mock stars are grouped by their [Fe/H] and [O/α] values. The stars with [O/α] $>$ 0 are hereafter referred to as high-O stars and the stars with [O/α] $<$ 0 as low-O stars. Generally, high-O stars have younger ages based on OEM models, while low-O stars become older. The effect of oxygen enhancement on age determination is relatively significant for stars with [Fe/H] $<$ -0.2. At [O/α] $=$ -0.2, the mean fractional age difference $((\tau_{\rm OEM}-\tau_{\alpha\rm EM})/\tau_{\alpha\rm EM})$ is 10.5% for metal-rich stars (-0.2 $<$ [Fe/H] $<$ 0.2) and 15.5% for relatively metal-poor stars (-1 $<$ [Fe/H] $<$ -0.2). The mean fractional age difference at [O/α] $=$ 0.2 is -9.2% for metal-rich stars and -16.5% for relatively metal-poor stars. The largest fractional age difference comes from high-O stars with [O/α]=0.4, which have a mean fractional age difference of -20.2% at -0.2 $<$ [Fe/H] $<$ 0.2 and -30.6% at -1 $<$ [Fe/H] $<$ -0.2. We find clear age offsets that correlate to the [Fe/H] and [O/α] values. Increasing 0.2 dex in [O/α] will reduce the age estimates of metal-rich stars by $\sim$10% and metal-poor stars by $\sim$15%. The mock data provide us with more sufficient stars at the metal-poor edge than observational data to present clearly age differences at different [O/α] and [Fe/H] values.

4.1.2. Observational Data

Figure 8 presents the fractional age differences between α EM and OEM models for observational (LAMOST and GALAH) and mock data. The overall average age offset (absolute value of age difference) of stars from LAMOST and GALAH is 8.9% and 8.6%, respectively. Of the low-O stars with [Fe/H] $<$ 0.1 dex and [O/α] $\sim$$-0.2$ dex, many have fractional age differences of $\geqslant$ 10% and even reach up to 27%. The mean fractional age difference of high-O stars with [O/α] $\sim$0.4 dex is $\sim$$-25$%. The age offsets are relatively significant for metal-poor stars. The largest age differences are -33% to

[13] For a certain star, age $-$ 2*age_uncertainty $>$ 13.8 Gyr.

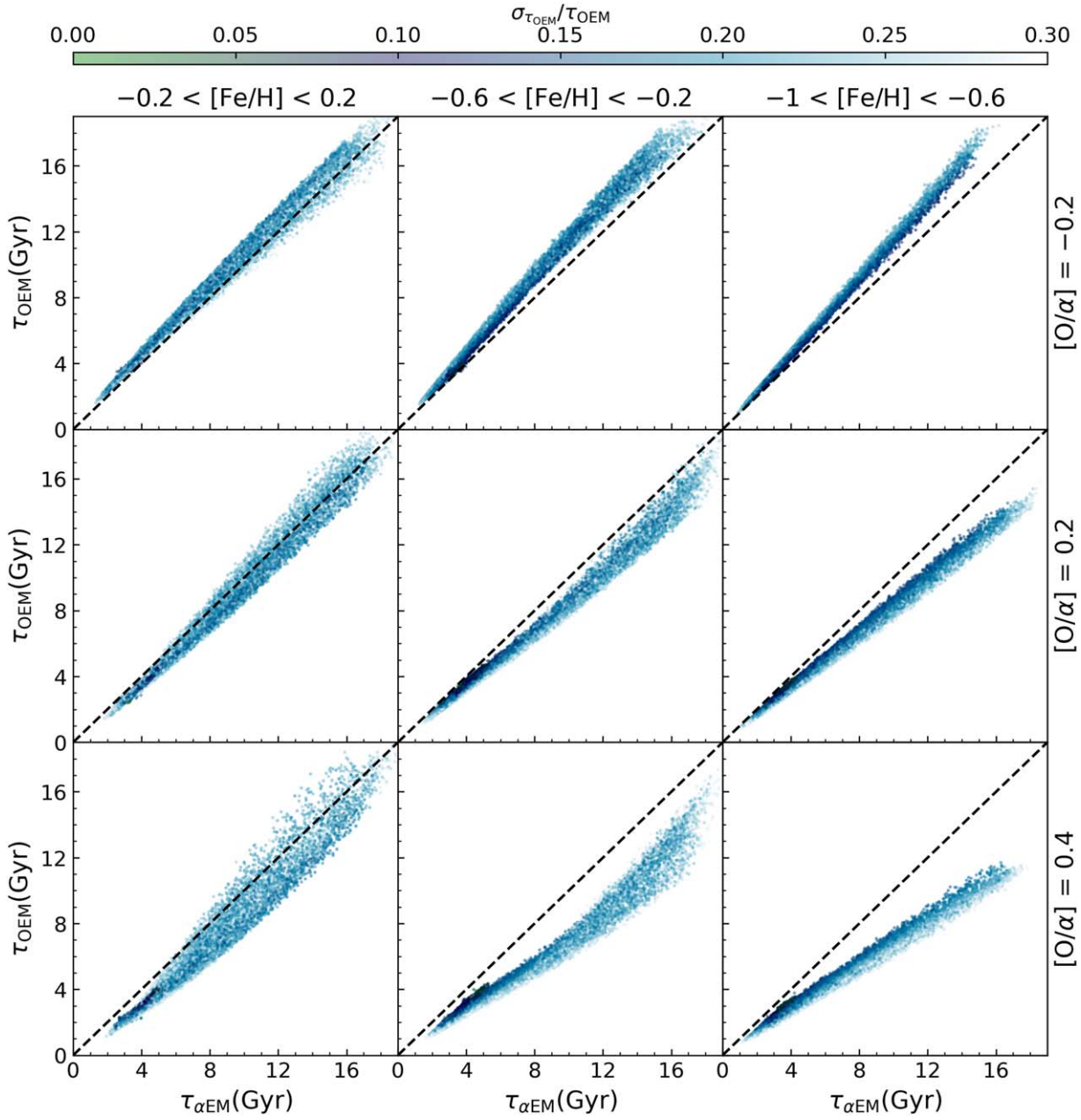

Figure 7. Comparison of the ages determined with α EM and OEM models for mock stars, color-coded by age uncertainty. These stars are divided by their [Fe/H] and [O/α] values. Black dashed lines show the agonic line.

-42% for stars with [Fe/H] $\lesssim -0.6$ dex and [O/α] $\sim$0.4 dex. For mock data, we note the trend of age offsets versus [Fe/H] is consistent with that of observational data. The age offsets of both samples increase significantly with decreasing metallicity at [Fe/H] $\gtrsim -0.6$. Interestingly, there is a slight increase in age offsets with decreasing metallicity at [Fe/H] < -0.6. This trend of age offsets is consistent with the change of $T_{\rm eff}$ difference as a function of [Fe/H] (shown in Figure 2), as discussed in Section 3.2.

4.2. Age–Abundance Relations

To trace the chemical evolution history of the Galactic disk, we hereby present the age–abundance relations of the LAMOST sample (consisting of 67,511 stars) and the GALAH sample (consisting of 4006 stars) using the ages from OEM models. For each sample, we employ local nonparametric regression fitting (LOESS model) to characterize the trends in these relations with enhanced clarity.

Figure 9 illustrates the results for the LAMOST sample. In Figure 9(a), a gradual decline in [Fe/H] is observed across the age range of $\sim$9 Gyr to $\sim$6.5 Gyr. This trend shows similarities to the metal-rich branch observed in young stars (age $<$ 8 Gyr) as found by Xiang & Rix (2022), where the metallicity range of their metal-rich branch stars spans approximately -0.2 to $+0.4$. Notably, Sahlholdt et al. (2022) also identifies a trend comparable to our findings, whereby their sample exhibits an [Fe/H] value of 0.4 at 8 Gyr, diminishing to around -0.2 at 6 Gyr. The "two-infall" chemical evolution model (Chiappini et al. 1997; Grisoni et al. 2017) predicts a process involving the infall of metal-poor gas commencing roughly 9.4 Gyr ago (Spitoni et al. 2019, 2020). The observed trend of decreasing

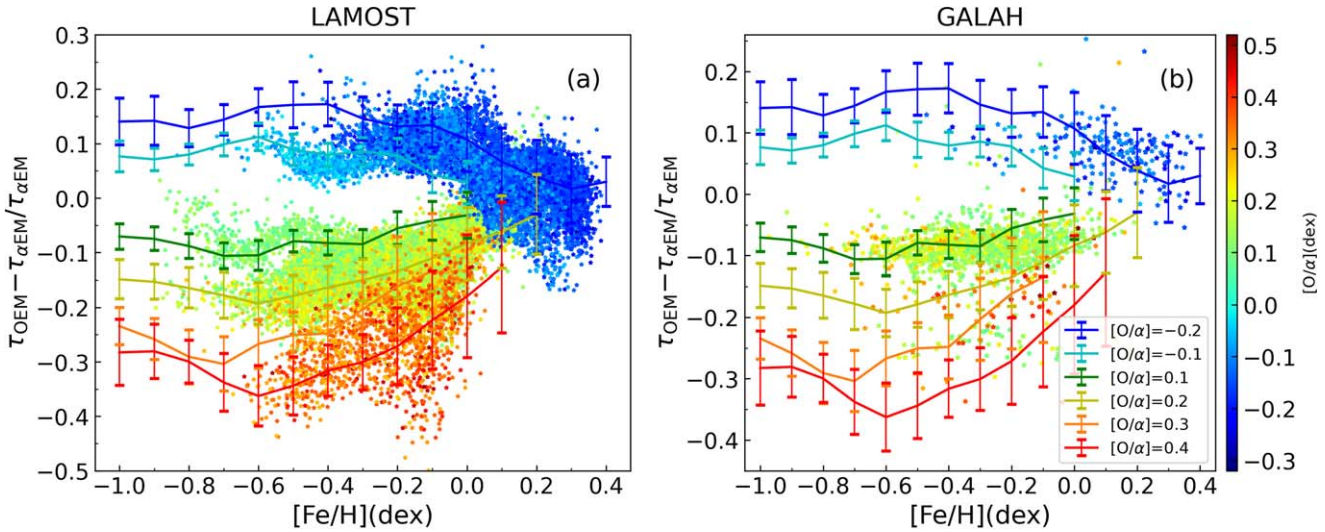

Figure 8. Distribution of fractional age difference as a function of [Fe/H] for sample stars from LAMOST (a) and GALAH (b), color-coded by [O/α]. The overplotted solid lines represent the median and standard deviation of fractional age difference for fake stars in each [Fe/H] bin, with a bin size of 0.1 dex.

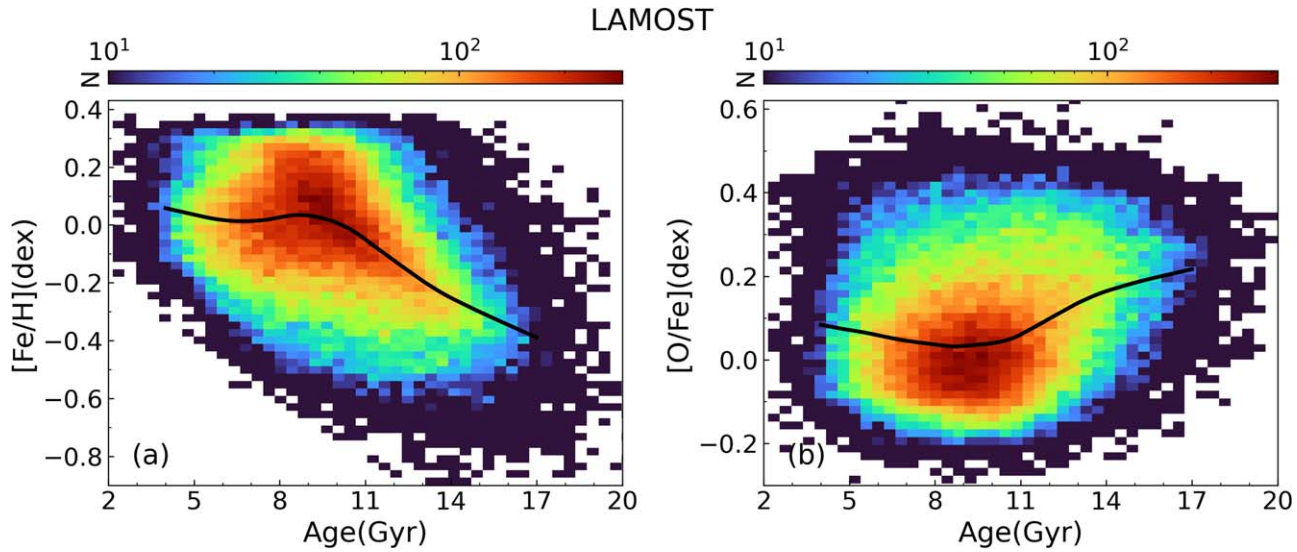

Figure 9. Color-coded stellar number density distribution of the sample stars from LAMOST in the age–[Fe/H] (a) and age–[O/Fe] (b) plane. The black solid lines represent the fitting for age–abundance relations by local nonparametric regression.

metallicity from 9 to 6.5 Gyr in our results may be related to this infalling metal-poor gas. Intriguingly, this "two-infall" model not only anticipates a decline in metallicity but also predicts an increase in the oxygen abundance, which is consistent with the observed trend illustrated in Figure 9(b). In Figure 9(b), the sample stars from LAMOST exhibit an increase in [O/Fe] as the age decreases from 9 to 4 Gyr, indicating a slight enrichment of oxygen in the younger stellar population.

Figure 10 presents the results for the GALAH sample. It is noteworthy that the GALAH stars display a decrease in [Fe/H] from ∼7.5 to 5 Gyr. Furthermore, the [O/Fe] of the GALAH stars exhibits a slight decrease with ages ranging from ∼7.5 to 3 Gyr. The GALAH sample exhibits age–[Fe/H] and age–[O/Fe] trends similar to those observed in LAMOST; however, an overall slight temporal discrepancy can be observed. This incongruity may be ascribed to dissimilarities in sample composition or systematic differences in atmospheric parameters between the two survey data sets. The GALAH sample, on the whole, exhibits higher temperatures compared to the LAMOST sample (5000–5700 K), indicating a relatively younger population. Furthermore, the determinations of [Fe/H] and [O/Fe] from GALAH are based on an NLTE method (Amarsi et al. 2020), which can also impact the observed trends.

In conclusion, the analysis of the LAMOST and GALAH samples reveals a decreasing trend of [Fe/H] with an age ranging from 7.5–9 Gyr to 5–6.5 Gyr and a notable upward trend in [O/Fe] as the age decreases from 7.5–9 Gyr to 3–4 Gyr. These results agree with the prediction of the "two-infall" scenario and suggest that a metal-poor and O-rich gas gradually dominates the star formation from 7.5 to 9 Gyr ago. As discussed in Section 1, oxygen has a unique origin, primarily produced by CCSNe (Franchini et al. 2021). Consequently, the observed age–[O/Fe] trend plays a distinct role in characterizing the chemical evolution history of the Milky Way and constraining chemical evolution models. Neglecting to account for the independent enhancement of

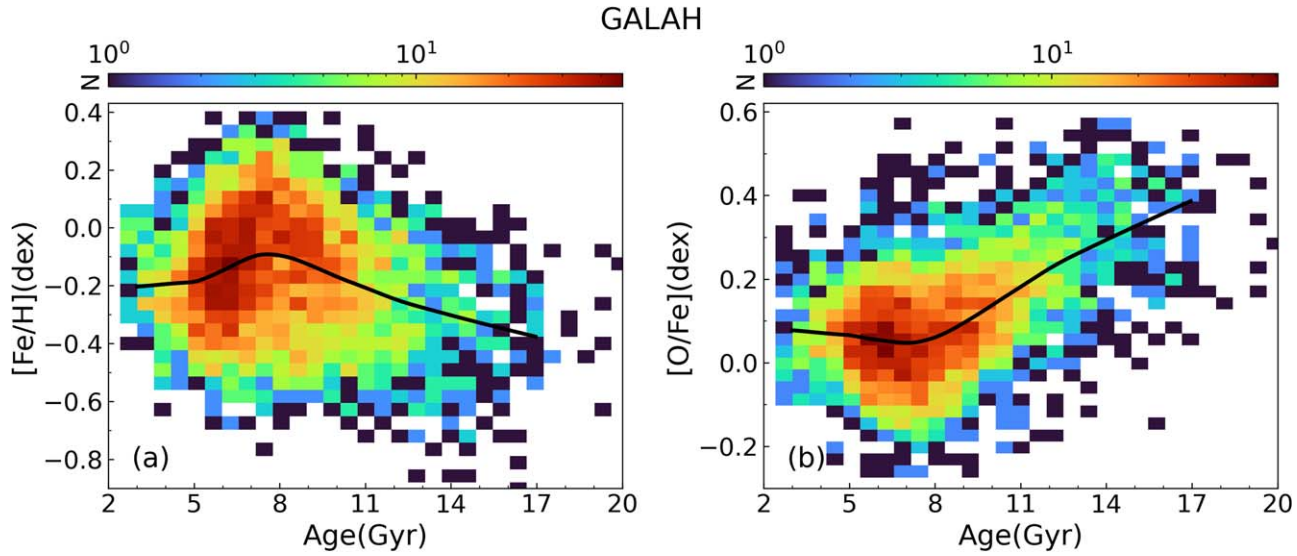

Figure 10. Color-coded stellar number density distribution of the sample stars from GALAH in the age–[Fe/H] (a) and age–[O/Fe] (b) planes. The symbols are the same as those defined in Figure 9.

oxygen abundance in age determination would result in significant age biases, as discussed in Section 4.1. Such biases would obscure the age–[O/Fe] relation, as depicted in Figure 12 in the Appendix, where the rising trend of [O/Fe] with decreasing age remains imperceptible at age <9 Gyr. Therefore, we suggest that considering the oxygen abundance independently in stellar models is crucial. This would aid in accurately characterizing the age–[O/Fe] relation and provide better constraints for Galactic chemical evolution models.

5. Conclusions

To determine the ages of dwarfs considering observed oxygen abundance, we construct a grid of stellar models, which take into account oxygen abundance as an independent model input. We generate mock data with 0.15 million mock stars to systematically study the effect of oxygen abundance on age determination. Based on the α-enhanced models and O-enhanced models, we obtain the masses and ages of 67,503 stars from LAMOST and 4006 stars from GALAH and analyze the chemical and kinematic properties of these stars combined with ages from O-enhanced models.

Our main conclusions are summarized as follows:

(i) The ages of high-O stars based on O-enhanced models are smaller compared with those determined with α-enhanced models, while low-O stars become older. We find clear age offsets that correlate to the [Fe/H] and [O/α] values. Varying 0.2 dex in [O/α] will alter the age estimates of metal-rich ($-0.2 <$ [Fe/H] < 0.2) stars by $\sim$10% and relatively metal-poor ($-0.2 <$ [Fe/H] < 0.2) stars by $\sim$15%.

(ii) The overall average age offset (absolute value of age difference) between α-enhanced models and O-enhanced models is 8.9% for LAMOST stars and 8.6% for GALAH stars. Of the low-O stars with [Fe/H] < 0.1 dex and [O/α] ~ -0.2 dex, many have fractional age differences of $\geqslant$ 10% and even reach up to 27%. The mean fractional age difference of high-O stars with [O/α] $\sim$0.4 dex is $\sim -25\%$ and reach up to -33% to -42% at [Fe/H] $\lesssim -0.6$ dex.

(iii) Based on LAMOST and GALAH samples, we observe a decreasing trend of [Fe/H] with ages from 7.5–9 Gyr to 5–6.5 Gyr. Furthermore, The [O/Fe] of both sample stars increases with decreasing age from 7.5–9 Gyr to 3–4 Gyr, which indicates that the younger population of these stars is more O rich. Our results agree with the prediction of the "two-infall" scenario and suggest that a metal-poor and O-rich gas gradually dominates the star formation from 7.5–9 Gyr ago.

Acknowledgments

We thank the anonymous referee for valuable comments and suggestions that have significantly improved the presentation of the manuscript. This work is based on data acquired through the Guoshoujing Telescope. Guoshoujing Telescope (the Large Sky Area Multi-Object Fiber Spectroscopic Telescope; LAMOST) is a National Major Scientific Project built by the Chinese Academy of Sciences. Funding for the project has been provided by the National Development and Reform Commission. LAMOST is operated and managed by the National Astronomical Observatories, Chinese Academy of Sciences. This work used the data from the GALAH survey, which is based on observations made at the Anglo Australian Telescope, under programs A/2013B/13, A/2014A/25, A/2015A/19, A/2017A/18, and 2020B/23. This work has made use of data from the European Space Agency (ESA) mission Gaia (https://www.cosmos.esa.int/gaia), processed by the Gaia Data Processing and Analysis Consortium (DPAC; https://www.cosmos.esa.int/web/gaia/dpac/consortium). Funding for the DPAC has been provided by national institutions, in particular the institutions participating in the Gaia Multilateral Agreement. This work is supported by National Key R&D Program of China No. 2019YFA0405503, the Joint Research Fund in Astronomy (U2031203,) under cooperative agreement between the National Natural Science Foundation of China (NSFC) and Chinese Academy of Sciences (CAS), and NSFC grants (12090040, 12090042). This work is partially supported by the CSST project, and the Scholar Program of Beijing Academy of Science and Technology (DZ:BS202002). This paper has received funding from the European Research Council (ERC) under the European Unions Horizon 2020 research and innovation program (CartographY GA. 804752).

Appendix

Figure 11 depicts the age and mass determinations for ∼15,000 LAMOST stars (with [α/Fe] ∼0.1) and reveals a satisfactory correspondence between the α EM models and the YY isochrones (Yi et al. 2008) as the dispersion of the relative age and mass differences are only 6.4% and 1.1% between these two models. However, slight systematic differences are visible among this result, as the YY yields 3.6% older age and −0.4% smaller mass than the α EM models.

Figure 12 shows the age–[O/Fe] relations of 67,503 LAMOST stars and 4006 GALAH stars, with the ages from α EM models.

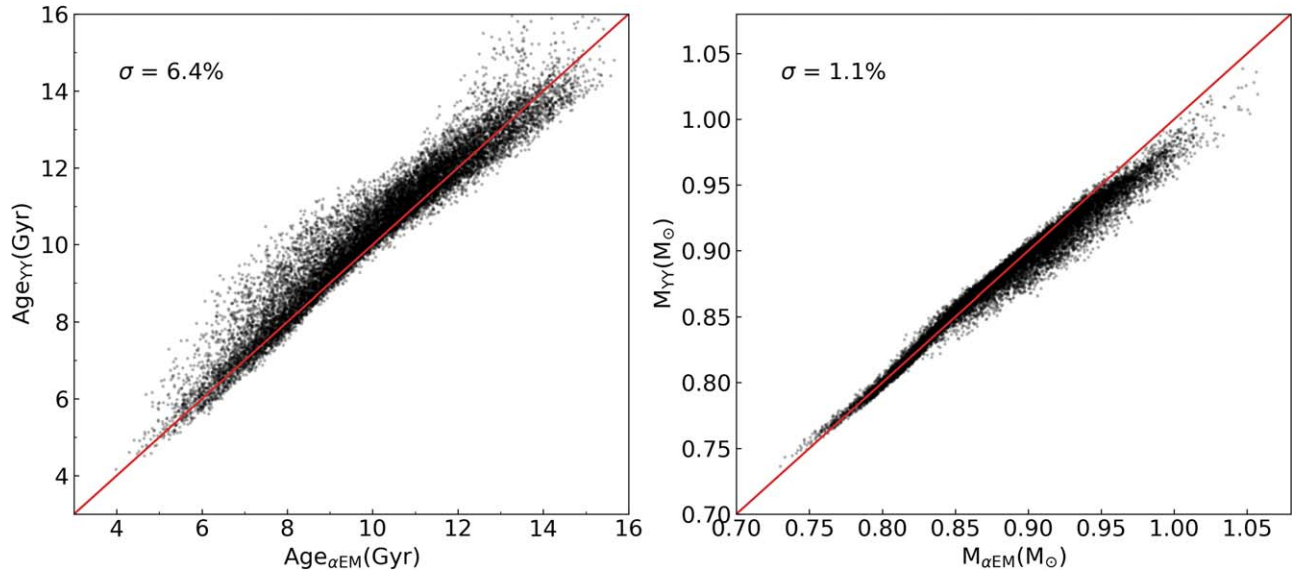

Figure 11. Comparison of age and mass estimates for ∼15,000 LAMOST stars using our α EM models and the YY (Yi et al. 2008) stellar isochrones with input [α/Fe] = 0.1 dex. The red line represents the 1:1 line. Dispersion of the relative age and mass difference are marked in the figure.

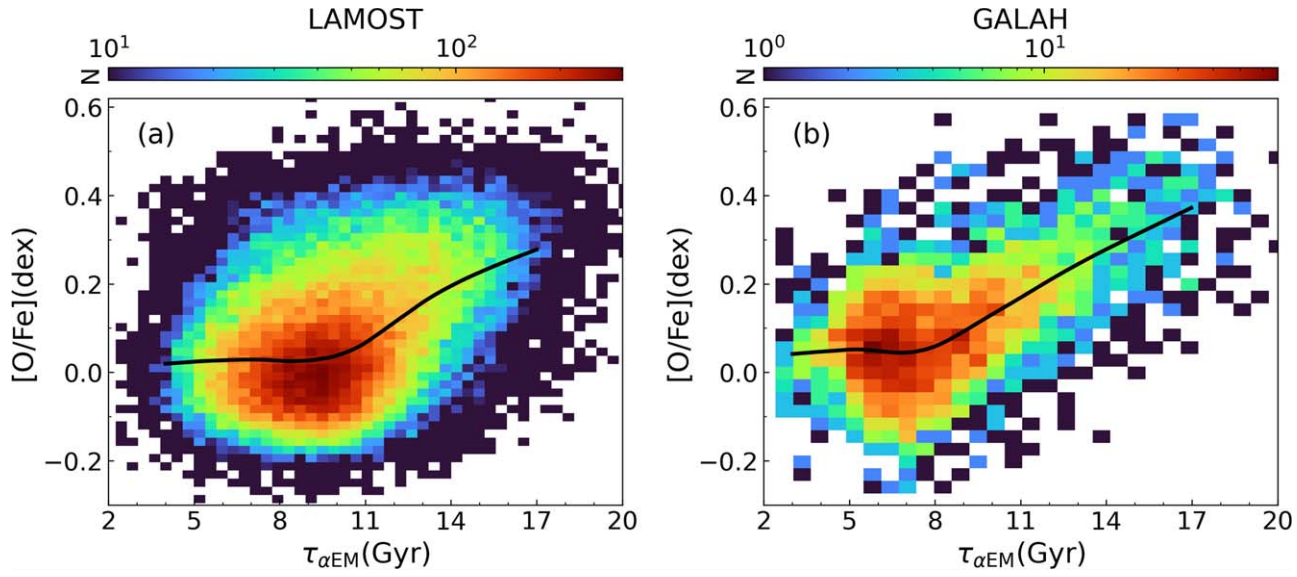

Figure 12. Color-coded stellar number density distribution of the sample stars from LAMOST (a) and GALAH (b) in the age–[O/Fe] plane, based on the ages from α EM models. The black solid lines represent the fitting for age–abundance relations by local nonparametric regression.

ORCID iDs

Tiancheng Sun https://orcid.org/0000-0003-0795-4854
Zhishuai Ge https://orcid.org/0000-0002-2614-5959
Xunzhou Chen https://orcid.org/0000-0003-3957-9067
Shaolan Bi https://orcid.org/0000-0002-7642-7583
Tanda Li https://orcid.org/0000-0001-6396-2563
Xianfei Zhang https://orcid.org/0000-0002-3672-2166
Yaguang Li https://orcid.org/0000-0003-3020-4437

References

Amarsi, A. M., Barklem, P. S., Asplund, M., Collet, R., & Zatsarinny, O. 2018, A&A, 616, A89
Amarsi, A. M., Lind, K., Osorio, Y., et al. 2020, A&A, 642, A62
Amarsi, A. M., Nissen, P. E., & Skúladóttir, Á. 2019, A&A, 630, A104
Angulo, C., Arnould, M., Rayet, M., et al. 1999, NuPhA, 656, 3
Bailer-Jones, C. A. L., Rybizki, J., Fouesneau, M., Demleitner, M., & Andrae, R. 2021, AJ, 161, 147
Basu, S., Chaplin, W. J., & Elsworth, Y. 2010, ApJ, 710, 1596
Bensby, T., Feltzing, S., Lundström, I., & Ilyin, I. 2005, A&A, 433, 185
Beom, M., Na, C., Ferguson, J. W., & Kim, Y. C. 2016, ApJ, 826, 155
Bertran de Lis, S., Delgado Mena, E., Adibekyan, V. Z., Santos, N. C., & Sousa, S. G. 2015, A&A, 576, A89
Bovy, J. 2015, ApJS, 216, 29
Bressan, A., Marigo, P., Girardi, L., et al. 2012, MNRAS, 427, 127
Buder, S., Sharma, S., Kos, J., et al. 2021, MNRAS, 506, 150
Carigi, L., Peimbert, M., Esteban, C., & García-Rojas, J. 2005, ApJ, 623, 213
Chaboyer, B., Fenton, W. H., Nelan, J. E., Patnaude, D. J., & Simon, F. E. 2001, ApJ, 562, 521
Chen, X., Ge, Z., Chen, Y., et al. 2020, ApJ, 889, 157
Chen, X., Ge, Z., Chen, Y., et al. 2022, ApJ, 929, 124
Chiappini, C., Matteucci, F., & Gratton, R. 1997, ApJ, 477, 765
Chugunov, A. I., Dewitt, H. E., & Yakovlev, D. G. 2007, PhRvD, 76, 025028
Cyburt, R. H., Amthor, A. M., Ferguson, R., et al. 2010, ApJS, 189, 240
Demarque, P., Woo, J.-H., Kim, Y.-C., & Yi, S. K. 2004, ApJS, 155, 667
Deng, L.-C., Newberg, H. J., Liu, C., et al. 2012, RAA, 12, 735
De Silva, G. M., Freeman, K. C., Bland-Hawthorn, J., et al. 2015, MNRAS, 449, 2604
Dotter, A., Chaboyer, B., Ferguson, J. W., et al. 2007, ApJ, 666, 403
Dotter, A., Chaboyer, B., Jevremović, D., et al. 2008, ApJS, 178, 89
Ferguson, J. W., Alexander, D. R., Allard, F., et al. 2005, ApJ, 623, 585
Franchini, M., Morossi, C., Di Marcantonio, P., et al. 2021, AJ, 161, 9
Freeman, K., & Bland-Hawthorn, J. 2002, ARA&A, 40, 487
Fu, X., Bressan, A., Marigo, P., et al. 2018, MNRAS, 476, 496
Fuller, G. M., Fowler, W. A., & Newman, M. J. 1985, ApJ, 293, 1
Gaia Collaboration, Vallenari, A., Brown, A. G. A., et al. 2023, A&A, 674, A1
Ge, Z. S., Bi, S. L., Chen, Y. Q., et al. 2016, ApJ, 833, 161
Ge, Z. S., Bi, S. L., Li, T. D., et al. 2015, MNRAS, 447, 680
Girardi, L., Bressan, A., Bertelli, G., & Chiosi, C. 2000, A&AS, 141, 371
Grevesse, N., & Sauval, A. J. 1998, SSRv, 85, 161
Grisoni, V., Spitoni, E., Matteucci, F., et al. 2017, MNRAS, 472, 3637
Helmi, A. 2020, ARA&A, 58, 205
Itoh, N., Hayashi, H., Nishikawa, A., & Kohyama, Y. 1996, ApJS, 102, 411
Kim, Y.-C., Demarque, P., Yi, S. K., & Alexander, D. R. 2002, ApJS, 143, 499
Kobayashi, C., Karakas, A. I., & Lugaro, M. 2020, ApJ, 900, 179
Kobayashi, C., Umeda, H., Nomoto, K., Tominaga, N., & Ohkubo, T. 2006, ApJ, 653, 1145
Langanke, K., & Martínez-Pinedo, G. 2000, NuPhA, 673, 481
Liu, X. W., Yuan, H. B., Huo, Z. Y., et al. 2014, in IAU Symp. 298, Setting the scene for Gaia and LAMOST, ed. S. Feltzing et al. (Cambridge: Cambridge Univ. Press), 310
Luo, A. L., Zhao, Y.-H., Zhao, G., et al. 2015, RAA, 15, 1095
Magrini, L., Randich, S., Kordopatis, G., et al. 2017, A&A, 603, A2
Majewski, S. R., Schiavon, R. P., Frinchaboy, P. M., et al. 2017, AJ, 154, 94
Maoz, D., Mannucci, F., & Brandt, T. D. 2012, MNRAS, 426, 3282
Marigo, P., Girardi, L., Bressan, A., et al. 2017, ApJ, 835, 77
Naiman, J. P., Pillepich, A., Springel, V., et al. 2018, MNRAS, 477, 1206
Nissen, P. E., Chen, Y. Q., Carigi, L., Schuster, W. J., & Zhao, G. 2014, A&A, 568, A25
Oda, T., Hino, M., Muto, K., Takahara, M., & Sato, K. 1994, ADNDT, 56, 231
Paxton, B., Bildsten, L., Dotter, A., et al. 2011, ApJS, 192, 3
Paxton, B., Cantiello, M., Arras, P., et al. 2013, ApJS, 208, 4
Paxton, B., Marchant, P., Schwab, J., et al. 2015, ApJS, 220, 15
Paxton, B., Schwab, J., Bauer, E. B., et al. 2018, ApJS, 234, 34
Paxton, B., Smolec, R., Schwab, J., et al. 2019, ApJS, 243, 10
Pietrinferni, A., Cassisi, S., Salaris, M., Percival, S., & Ferguson, J. W. 2009, ApJ, 697, 275
Planck Collaboration, Ade, P. A. R., Aghanim, N., et al. 2016, A&A, 594, A13
Pols, O. R., Tout, C. A., Eggleton, P. P., & Han, Z. 1995, MNRAS, 274, 964
Potekhin, A. Y., & Chabrier, G. 2010, CoPP, 50, 82
Reddy, B. E., Lambert, D. L., & Allende Prieto, C. 2006, MNRAS, 367, 1329
Rogers, F. J., & Nayfonov, A. 2002, ApJ, 576, 1064
Sahlholdt, C. L., Feltzing, S., & Feuillet, D. K. 2022, MNRAS, 510, 4669
Salasnich, B., Girardi, L., Weiss, A., & Chiosi, C. 2000, A&A, 361, 1023
Saumon, D., Chabrier, G., & van Horn, H. M. 1995, ApJS, 99, 713
Schönrich, R., Binney, J., & Dehnen, W. 2010, MNRAS, 403, 1829
Sharma, S., Stello, D., Buder, S., et al. 2018, MNRAS, 473, 2004
Soderblom, D. R. 2010, ARA&A, 48, 581
Spitoni, E., Silva Aguirre, V., Matteucci, F., Calura, F., & Grisoni, V. 2019, A&A, 623, A60
Spitoni, E., Verma, K., Silva Aguirre, V., & Calura, F. 2020, A&A, 635, A58
Thoul, A. A., Bahcall, J. N., & Loeb, A. 1994, ApJ, 421, 828
Timmes, F. X., & Swesty, F. D. 2000, ApJS, 126, 501
Ting, Y.-S., Conroy, C., Rix, H.-W., & Asplund, M. 2018, ApJ, 860, 159
Ting, Y.-S., Rix, H.-W., Conroy, C., Ho, A. Y. Q., & Lin, J. 2017, ApJL, 849, L9
Traven, G., Feltzing, S., Merle, T., et al. 2020, A&A, 638, A145
Vandenberg, D. A. 1992, ApJ, 391, 685
VandenBerg, D. A., Bergbusch, P. A., Dotter, A., et al. 2012, ApJ, 755, 15
Ventura, P., D'Antona, F., Imbriani, G., et al. 2018, MNRAS, 477, 438
Wheeler, J. C., Sneden, C., & Truran, J. W. J. 1989, ARA&A, 27, 279
Xiang, M., & Rix, H.-W. 2022, Natur, 603, 599
Xiang, M., Ting, Y.-S., Rix, H.-W., et al. 2019, ApJS, 245, 34
Yi, S., Demarque, P., Kim, Y.-C., et al. 2001, ApJS, 136, 417
Yi, S. K., Kim, Y.-C., & Demarque, P. 2003, ApJS, 144, 259
Yi, S. K., Kim, Y.-C., Demarque, P., et al. 2008, in IAU Symp. 252, The Art of Modeling Stars in the 21st Century, ed. L. Deng & K. L. Chan (Cambridge: Cambridge Univ. Press), 413
Zhao, G., Zhao, Y.-H., Chu, Y.-Q., Jing, Y.-P., & Deng, L.-C. 2012, RAA, 12, 723
Zwitter, T., Kos, J., Buder, S., et al. 2021, MNRAS, 508, 4202